1 **Supplemental Data**

2 *Section S1: Selection of IM*

3   Several studies have examined different IMs for buildings (e.g. Luco and Cornell 2007; Eads

4 et al. 2015) and bridges (e.g. Mackie and Stojadinovic 2004; Padgett et al. 2008) and their

5 suitability for use in IDA. For individual bridges, previous studies on this topic recommend use of

6 elastic spectral acceleration (Sa) at a period of ~1.3 × fundamental period, because bridges have

7 many sacrificial elements, after failure of which, the stiffness significantly decreases and hence

8 the fundamental period elongates (Mackie and Stojadinovic 2004). For suites of bridges, PGA has

9 been considered as a representative IM (Padgett et al. 2008). Sa_{avg} (Eads et al. 2015) and other IMs

10 that quantify spectral shape can resolve the problem with period elongation.

11   For these reasons, the present study focused especially on evaluating Sa_{avg} as an IM. As this

12 study is concerned with 3D models of bridges, the authors also evaluated these IMs in terms of

13 different methods of combining the ground motion characteristics in the two orthogonal directions:

14 arithmetic mean, geometric mean, square root of the sum of the squares (SRSS), and maximum

15 component (i.e. taken as large of IM values in the horizontal directions).

16   Table S1 shows the 81 scalar IMs considered here, which include possible combinations of

17 Sa_{avg} considered as an IM; each IM is derived by combining selections from each column in the

18 table (with the selected combination in red). The period range was varied between 0.2T-3.0T

19 (recommended by (Eads et al. 2015)) to 0.8T-1.5T. The authors used two different methods to

20 determine the period range of interest in each direction. In the first case, the authors used

21 fundamental period of the bridge to calculate the Sa_{avg} in both directions, i.e. the value of period

22 to calculate period ranges was the same in both directions. In the second case, the Sa_{avg} in each

23 direction was determined using the first period in the given direction, i.e. the value of period to

24 calculate period ranges was different for each direction. The total number of combinations in the

25 table is 80. In addition, the authors also examined Sa at the fundamental period, making the total

26 number of IMs 81. The IMs are evaluated in terms of (i) *proficiency*, a composite measure of the

27 sensitivity of EDPs to changes in the values of IM (termed *practicality*), and the variance in the

28 estimated EDP for a given IM (termed *efficiency*) (Padgett et al. 2008), and (ii) *sufficiency*, a

29 measure of the statistical independence of the IM from earthquake and ground motion parameters,

30 such as magnitude and distance (Luco and Cornell 2007).

31 Each IM was evaluated based on the proficiency with respect to the EDPs governing column

32 and abutment response identified by Padgett et al. (2008), considering compression strain in

33 concrete cover, residual drift, maximum displacement of shear keys, and displacement of

34 backwall. These EDPs are very highly correlated with rest of the EDPs, so the authors assumed

35 that the performance of IM with these selected EDPs would be very similar to its performance

36 with rest of the EDPs. The authors then ranked the IMs based on how they performed with each

37 of the governing EDPs and selected the overall best performing IM (shown in bold in Table S1).

38 The authors found this IM to be sufficient with respect to source distance and earthquake

39 magnitude (using p-value of 0.05) following the recommendations of Luco and Cornell (2007).

40 **Table S1.** Different versions of Sa_{avg} considered as IM, with selected version in bold

| Period region	Period	Combination
First period	Fundamental	Max. component
0.2T – 3.0T	**First period in each direction**	**Arithmetic mean**
0.5T – 3.0T		Geometric mean
0.8T – 3.0T		SRSS
0.2T – 2.25T		
0.5T – 2.25T		
0.8T – 2.25T		
0.2T – 1.5T		
0.5T – 1.5T		
0.8T – 1.5T		

41

42   *Section S2: Correlation of EDPs*

43   The structural response simulation shows that several of the EDPs are strongly correlated. Two

44   trends in dependence are observed: linear and bilinear. The authors often observed a linear trend

45   between EDPs of same and related components (e.g. strains in plastic hinges of columns). A

46   bilinear trend was often observed between EDPs of non-related elements. The bilinear trend is

47   caused by rapid change in resistance of one (or both) of the elements. Examples of linear and

48   bilinear correlations are shown in Fig. S1. Accounting for these correlations is necessary in order

49   to prevent generating "unreasonable" combinations of EDPs in MCS.

50   In the case of linear correlation, MCS generates correlated EDPs using a correlation matrix

51   derived from the simulation results. In the case of bilinear dependence, a bilinear model is fitted

52   to the data. Then, for each generated point of the independent variable, the one or more dependent

53   variables are taken from the distribution calculated from the appropriate bilinear model. This

54   distribution has a mean value that corresponds to the value predicted by the bilinear model, and a

55   standard deviation that corresponds to the standard deviation of whichever branch of the bilinear

56   model applies. Examples of both trends are presented in Fig. S1. It is noted that the linear model

57   is not shown in Fig. S1a, because it is not needed for MCS (the correlation matrix is used to

58   simulate the linearly correlated EDPs).

59

60   a)   b)
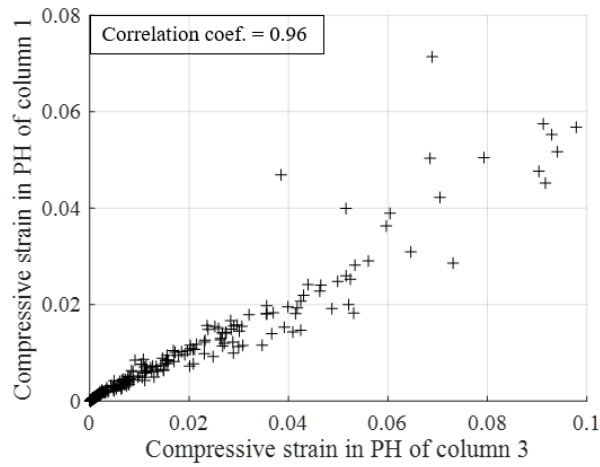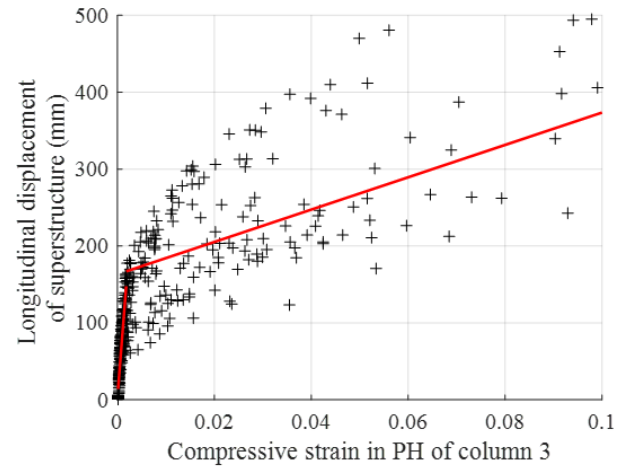
61   **Fig. S1.** Examples of linear and bilinear correlations: a) linear correlation between compressive strains in

62   plastic hinges of column 3 and 1 of PB1, and b) bilinear correlation between strain in PH of column 3 and

63   displacement of superstructure (into backwall) of PB1

64 *Section S3: Bridge geometry*

65   The National Bridge Inventory (FHWA 2015) shows that most bridges built since 2000 in

66   California have continuous (26%) or simply (28%) supported prestressed (including post-

67   tensioning) concrete superstructures. Most of the multi-span bridges (56%) are built with

68   continuous prestressed concrete superstructure using a multiple box-girder design. The trends in

69   construction and geometry of selected bridges are shown in Table S2.

70   **Table S2.** Properties of California bridges constructed since 2000, compared to prototype bridges

|	Mean	Standard deviation	PB1	PB2
Number of spans (main unit)	3	2	3	2
Number of spans (total)	3	2	5	2
Span length [m] (ft)	44 (144)	14 (45)	30 (100) (approach 24 (80))	47 (155)
Total length [m] (ft)	125 (411)	105 (344)	140 (460)	94 (310)
Superstructure width [m] (ft)	20 (67)	10 (32)	12 (39)	23 (75)
Under-clearance [m] (ft)	6 (21)	2 (7)	7 (22)	7 (22)

71

72   PB1 was designed by professional engineers for purposes of their study, but was not built. PB2

73   was built in 2001 and is located in Orange, CA. Table S3 shows properties of PB1 and PB2. The

74   superstructure cross-sections of PB1 and PB2 are provided in Fig. S2. The design values of PGA

75   for PB1 and PB2 are 0.49 g and 0.40 g. These values are equivalent to $\overline{Sa_{avg}}$ values of 0.49 g and

76   0.43 g.

77

78

Table S3. Prototype bridge geometry

Parameters	PB1	PB2
General bridge description	Ordinary standard single-column bent bridge with 5 spans	Ordinary standard multi-column bent bridge with 2 spans
Total length of the bridge	141 m (460 ft)	94 m (310 ft)
Length of each span	25 m (80 ft) approach and 31 m (100 ft) main spans	47 m (155 ft)
Total superstructure width	12 m (39 ft)	23 m (75.5 ft)
Superstructure depth	1.2 m (4 ft)	1.9 m (6.23 ft)
Superstructure type	Post-tensioned concrete box girder	RC box girder
Number of bents	4	1
Number of columns	4	2
Clear height of each column	6.7 m (22 ft)	6.7 (22 ft)
Column diameter	1.2 m (4 ft)	1.7 m (5.58 ft)
Length of the cap beam (c. to c.)	NA	11 m (36 ft)
Cap beam dimensions	NA	2.3 m x 1.9 m (7.55 ft x 6.23 ft)
Seat width	762 mm (30 in)	762 mm (30 in)
Location of expansion joints	No joints specified	No joints specified
Column-to-foundation connectivity	Fixed	Pinned (two-way hinge)
Nominal concrete strength for superstructure	27.5 MPa (4 ksi)	27.5 MPa (4 ksi)
Nominal concrete strength for bents	34.5 MPa (5 ksi)	34.5 MPa (5 ksi)
Column longitudinal reinforcement	14 #10	44 #11 bundled
Column transverse reinforcement	#6 at 5 in pitch	#6 at 5 in pitch

79

80

81
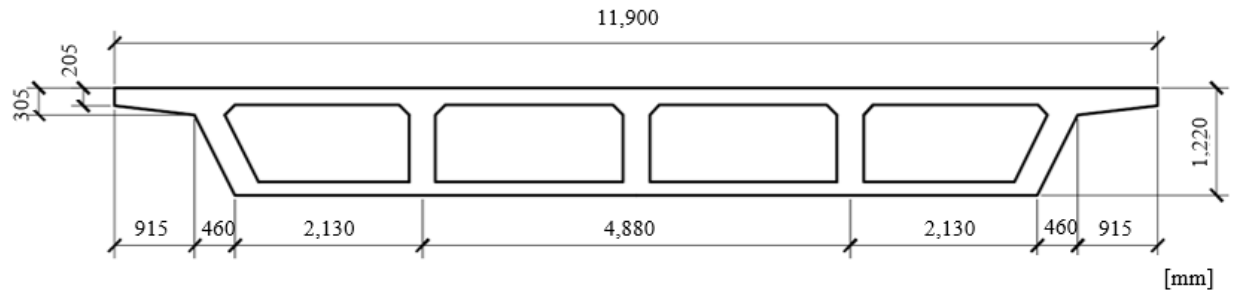
82   a)
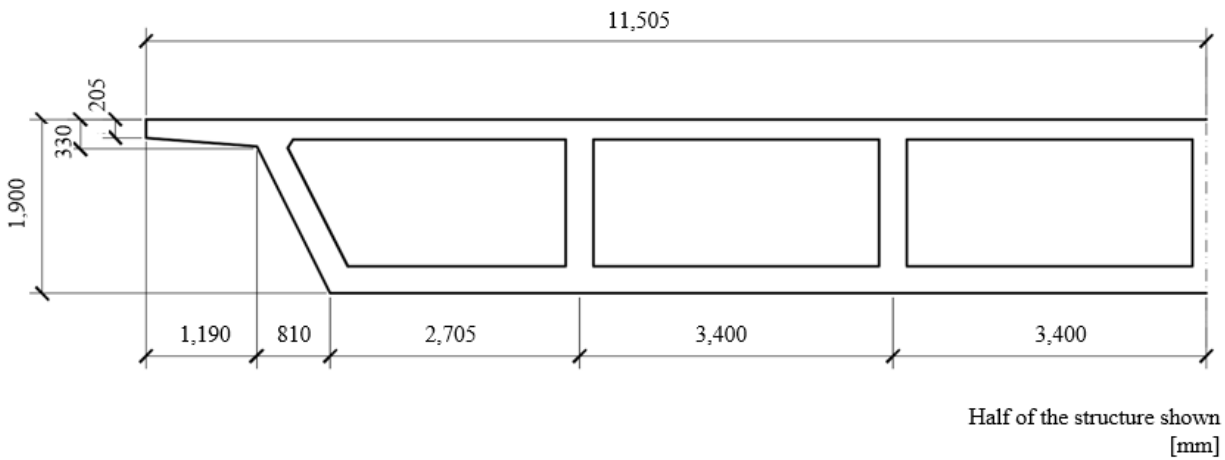
Half of the structure shown
[mm]

83

84   b)

85   **Fig. S2.** Superstructure geometry of: a) PB1 and b) PB2

86   The foundation of PB1 consists of a 2x2 pile group of circular open-ended steel pipes (PP 24

87   x 0.5) with length of 18.5 m (60.5 ft). In the case of PB2, each column is supported on a 4x5 pile

88   group of cast-in-drilled-hole concrete piles with diameter of 600 mm (23.5 in) and length 3 m (10

89   ft). The stiffness for the springs in nonlinear model is taken from Ketchum et al. (2004).

90   In the longitudinal direction, superstructure translation is resisted by the backwall and backfill.

91   A gap is designed between abutment backwall and superstructure to accommodate movement

92   caused by temperature variations, and post-tensioning strand relaxation (for PB1). The movement

93   rating is the total anticipated movement from widest to narrowest opening of a joint (Caltrans,

94   1994). Hence, the gap between the superstructure and backwall only needs to accommodate half

95   of movement rating plus some extra width for attachment of seals or seal assemblies. The

96   movement ratings for the bridges are calculated as 75 mm (3 in), and 50 mm (2 in) for PB1 and

97   PB2, respectively, which requires a joint seal assembly (i.e. an assembly of steel profiles and seals

98   required in cases of large movement ratings) for PB1, and Type B seals for PB2 to fill the gap

99   (Caltrans 1994b). The gaps between superstructure and backwall at either end of the bridge are 50

100   mm (2 in), and 25 mm (1 in), for PB1 and PB2, respectively, to accommodate the bridge movement

101   rating.

102   The relative movement between the superstructure and the abutments is accommodated by

103   elastomeric bearings. The design of bearings consists of 5 bearings of 305 mm x 305 mm (12 in x

104   12 in) cross-section dimensions, and height of elastomer of 50 mm (2 in) for PB1, and of 7 bearings

105   of 580 mm x 580 mm (23 in x 23 in) cross-sectional dimensions, and height of elastomer of 50

106   mm (2 in) for PB2.

107

108   ***Section S4: Nonlinear modeling***

109   The behavior of each column is modeled using GI column elements (Salehi and Sideris 2017;

110   Sideris and Salehi 2016). The GI element formulation utilizes the GI beam theory to eliminate the

111   strain localization phenomena of the classical beam theory, thereby, providing prediction of strain

112   and curvature in plastic hinge locations and offering better convergence properties of the numerical

113   solution algorithm, compared to conventional flexibility-based elements. For each element, 13

114   control sections (integration points) are considered over its length, so that convergence

115   requirements per Sideris and Salehi (2016) are met. Each control section is divided into fibers. The

116   fibers in the section behave according to prescribed uniaxial stress-strain models. Each section

117   contains fibers representing: (i) confined core concrete, the response of which is modeled using

118   Mander et al. (1988)'s model via the *OpenSEES* Concrete04 material model, with residual strength

119   for strains higher than the crushing strain of 10% of the ultimate strength, (ii) unconfined cover

120   concrete, the response of which is modeled using the Concrete02 material model, and (iii) steel

121   (longitudinal) reinforcement.

122   For the steel reinforcement, a computationally-efficient material model that can capture both

123   rebar fracture and buckling was developed by the authors by modifying a simple bilinear damage

124   material model to incorporate a second bounding surface to represent rebar buckling in

125   compression. In the bilinear damage material model, a bounding surface is used to represent

126   yielding resulting in a response identical to kinematic plasticity. Fracture is captured through a

127   damage factor applied to bounding surface. The damage factor varies linearly with the peak

128   absolute strain over the entire response and is intended to capture strain softening and eventual

129   rebar fracture (i.e. complete loss of axial resistance). This damage factor provides a smooth

130   transition over the various regimes of response, permitting better convergence.

131   As part of this study, a second bounding surface was introduced to represent stress reduction

132   associated with rebar buckling. The "buckling" bounding surface is a function of the slenderness

133   ratio (ratio between buckling length and diameter of the bar), and yield strength and strain of

134   longitudinal rebar. This surface has a power form and has been developed via regression analysis

135   using 47 experiments of bare bars (Mander et al. 1994; Bayrak and Sheikh 2001; Bae et al. 2005).

136   The buckling length is calculated using the model proposed by Dhakal and Maekawa (2002) using

137   an energy method. Their study showed that their model predicts buckling length well for

138   rectangular columns, while Kashani et al. (2016) showed the same for circular columns. The

139   revised model was incorporated in the OpenSEES. A comparison of the buckling surface with

140   selected experimental results is shown in Fig. S3.

141
142
(a)   (b)

143
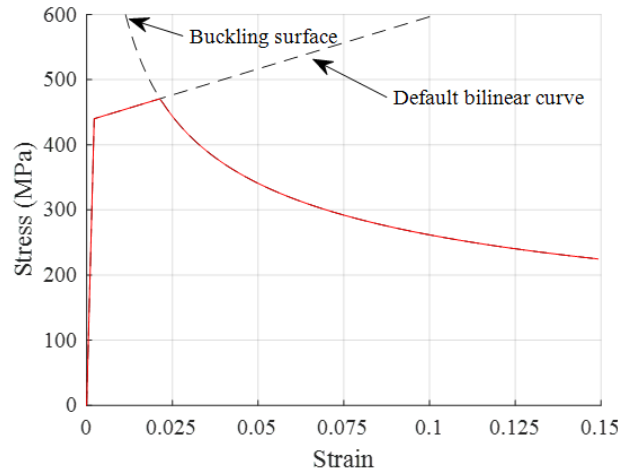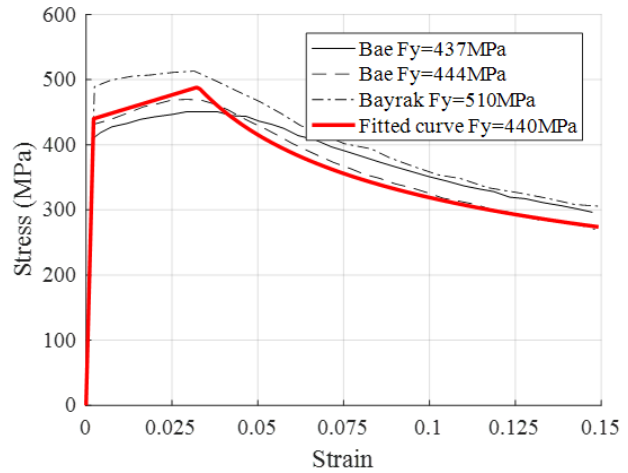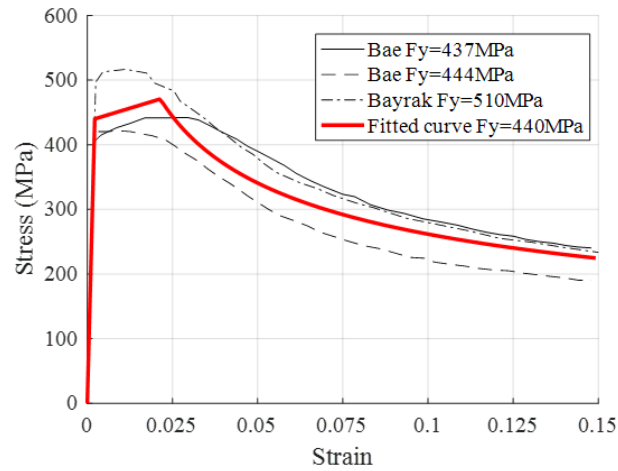
144   (c)   (d)
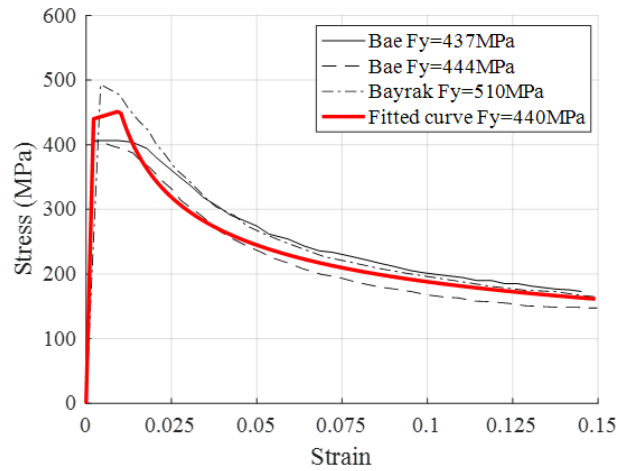145 **Fig. S3.** a) Rebar material model, b) – d) comparison of model to experimental results for slenderness

146   ratios of 6, 8, and 10, showing that model matches experimental data well

147   The concrete material models used in the original model and in bridge models repaired with

148 prestressed, steel, and RC jackets follow Mander et al. (1988)'s model, with model parameters

149 calculated based on confinement provided by the external jacket. The concrete material confined

150 by CFRP jacket follows an average of the models proposed by Jiang and Teng (2007) and Spoelstra

151 and Monti (1999). The behavior of CFRP is essentially linear until fracture. This causes the

152 concrete confined by CFRP jacket to not experience the softening behavior present at the rest of

153 the models due to yielding of transverse reinforcement or steel jacket. The stress-strain curves in

154 compression are shown in Fig. S4.

155

156   a)   b)
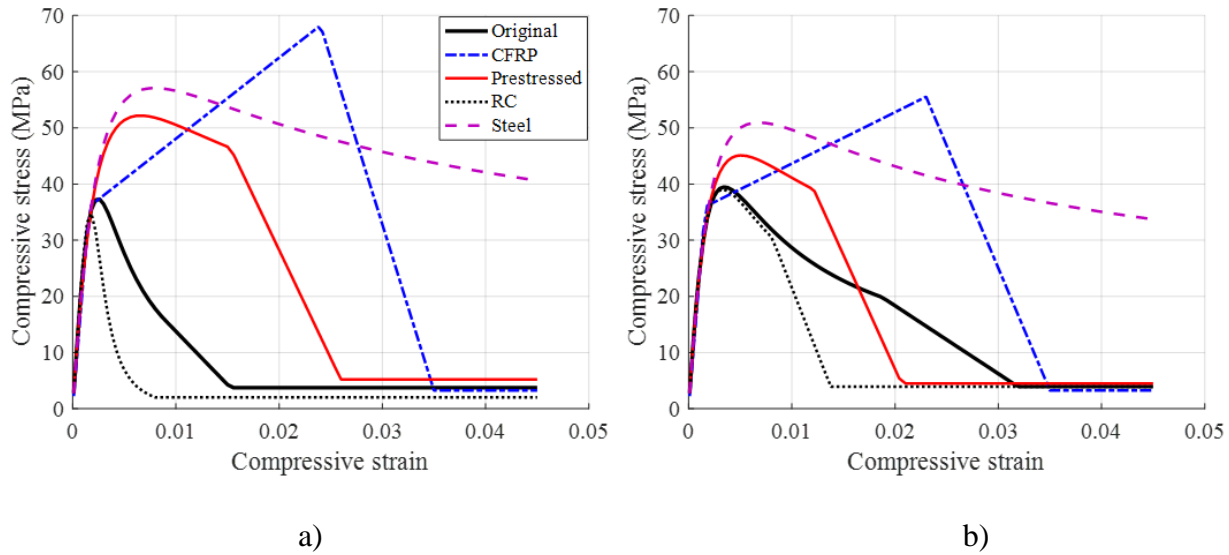
157   **Fig. S4.** Material behavior of confined concrete in compression for: a) PB1, and b) PB2

158   Additional rotational springs at the bottom and top of each column represent bar slip. Murcia-

159 Delso (2013) proposed a material model for a single embedded bar, which is used in this study to

160 obtain moment-rotation behavior of the bar slip spring. Specifically, we modeled each rebar as an

161 axial spring using Murcia-Delso bar slip material in tension, and very stiff response in the

162 compression, and subjected this assembly to increasing rotation. We then implemented the

163 obtained moment-rotation behavior into a rotational spring.

164   The bearings are modeled using the *OpenSEES* bearing elements. The bearing element uses

165 linear elastic material in all direction except for horizontal translation, for which a linear elastic,

166 perfectly plastic material is assigned. The material properties are obtained for elastomer Durometer

167 55 from manufacturer information materials (Goodco Z-Tech 2015).

168   Shear key and backwall behavior is modeled based on experimental data (Bozorgzadeh et al.

169 2006; Bozorgzadeh 2007; Stewart et al. 2007) by using available materials in *OpenSEES* and their

170   combinations in series. The models are compared in Fig. S5 to experimental data (F_{ult} in Fig. S5b

171   is defined as maximum horizontal force that the backwall can resist and is calculated from

172   geometry of the backwall and soil properties). Due to nature of the resistance provided by shear

173   keys and backwall-backfill, the models have only in-cycle deterioration, but not cyclic

174   deterioration. In both the transverse and the longitudinal direction, the physical gaps between

175   superstructure and shear keys, and superstructure and backwall, are represented in the model, but

176   not shown in the figure.

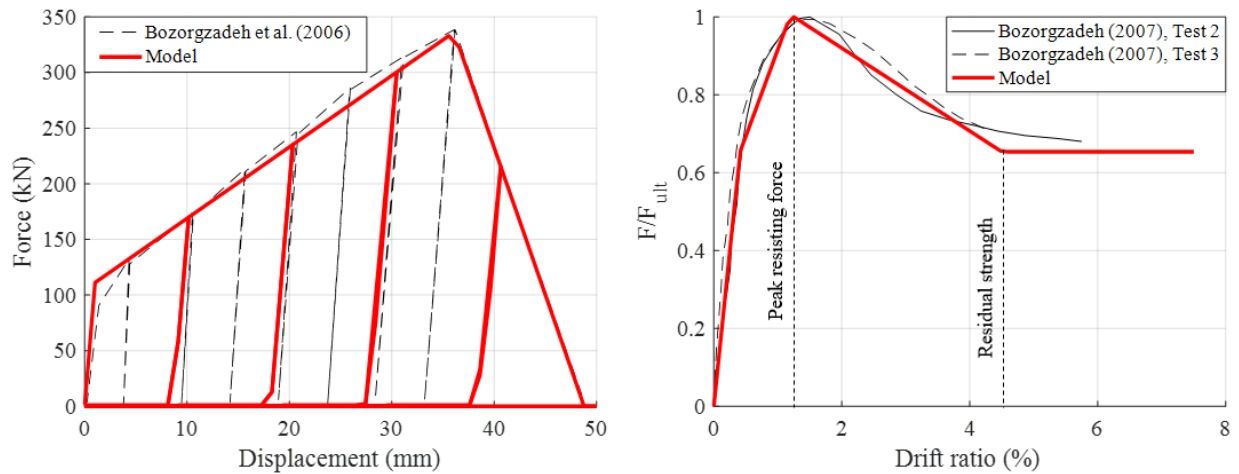178   (a)   (b)
179   **Fig. S5.** Behavior of a) shear keys, b) backwalls, with comparison to experimental data, showing both

180   models capture test data well

181   Note that the shear key and the backwall force-displacement response depends on the

182   displacement in the shear key or backwall itself and is measured after the gap between

183   superstructure and shear key/backwall closes, while the EDP for determining DS of shear

184   key/backwall is the transverse or longitudinal displacement of the superstructure, i.e. it includes

185   the gap size. Hence, the displacement at the gap closure needs to be added to the displacements

186   calculated from shear key/backwall lateral force-displacement behavior. The scheme and nonlinear

187   model of the seat abutment is shown in Fig. S6.

188   The stiffness values of the foundation springs were obtained for pile foundations based on

189   foundation stiffness analysis (Ketchum et al. 2004). They performed the analysis using nonlinear

190   p-y springs (relates net soil reaction per unit length and pile lateral deflection) representing soil

191   conditions. The analysis assumed shadowing effects in the pile groups by applying reduction factor

192   to the p-y springs.

ZL1 – Spring modeling Shear key
ZL2 – Spring modeling Bearings
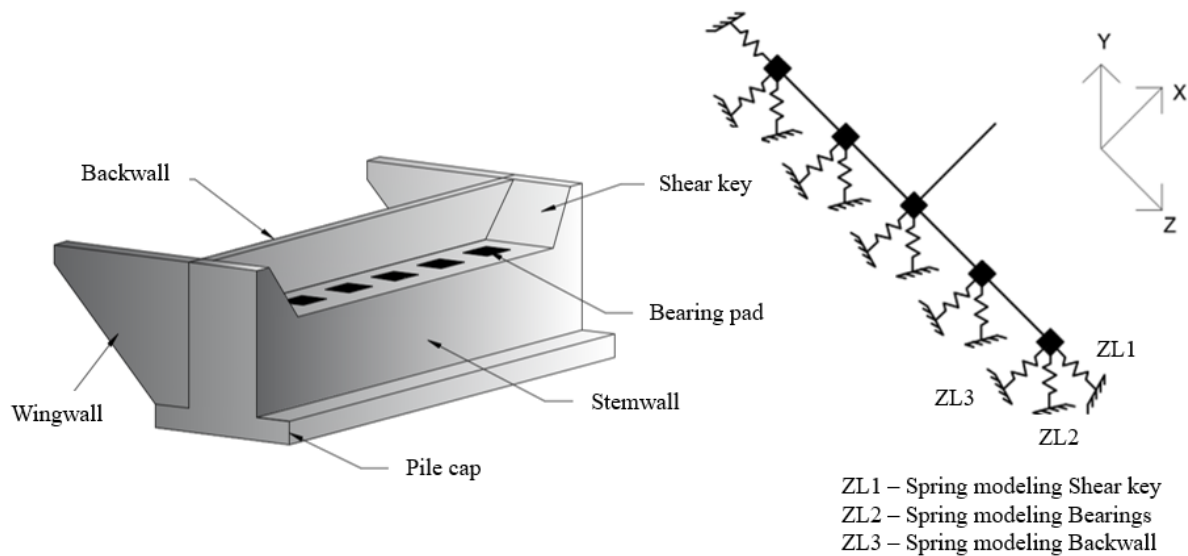ZL3 – Spring modeling Backwall

193
194   **Fig. S6.** Abutment and spring model representing abutment response

195   Modern code provisions ensure that for ordinary standard bridges, the superstructure remains

196   essentially elastic (AASHTO 2011; Caltrans 2013). To confirm this assumption, the yield capacity

197   of the superstructure, obtained from moment-curvature analysis, was compared to the maximum

198   moment demand during pushover analysis. The pushover analysis was performed in transverse

199   and longitudinal directions, and in both cases the demands were at least 10% below the

200   superstructure yield capacity. Hence, the superstructure is modeled using linear-elastic elements.

201   In the case of PB1, the superstructure is post-tensioned, so gross cross-sectional properties are used

202   in the model (Caltrans 2013). For PB2, cracked section properties are used (Aviram et al. 2008).

203   *Section S5: Abutment and superstructure damage states*

204   The abutment damage states are presented in Table S4. All displacements in column 3 (EDP)

205   refer to displacement of the superstructure; for shear keys they refer to displacement in transverse

206   direction, and for backwall they refer to displacement in longitudinal direction.

207   Slipping of bearings is limited by the friction force between the bearing and concrete. For this

208   study, the friction coefficient between concrete and neoprene is taken conservatively as 0.4

209   (Caltrans, 2013), although this coefficient can be higher due to gravity loads (Konstantinidis et al.

210   2008). The "roll-over" limit is reached when the originally vertical surface of the bearing comes

211   in contact with horizontal surface. This limit is reached at shear strains around 300%, and is the

212   governing limit state for stocky bearings. For slender bearings, the "roll-off" limit state can occur.

213   During this state, the unbonded loading surfaces of the bearing partially roll off the concrete

214   surface, and decrease the contact area between the bearing and girder or abutment stemwall. This

215   decrease in effective area decreases the stiffness (and can eventually reach zero, causing the

216   bearing to become unstable and fail). All three limit states should be checked. The governing

217   failure mode of the bearings for both PB1 and PB2 is slipping.

218   For shear keys, DS1 occurs when the gap between superstructure and shear key closes, DS2

219   when the deformation demand in the shear key is 25% of shear key's displacement capacity, DS3

220   at 60% of the displacement capacity, and DS4 (or failure) at 100% of the displacement capacity.

221   For backwall, DS1 occurs when the gap between superstructure and backwall exceeds the

222   limits of the seals, DS2 when the gap closes, DS3 when the backwall is at its peak resisting force

223   and the slip plane in backfill forms, and DS4 (or failure) when the backwall shears off.

224

225

Table S4. Abutment damage states

DS	Qualitative description	EDP	Median threshold PB1	Median threshold PB2	Log. (ln) std. dev. of threshold	Reference
			Bearing			
DS1	Slipping of bearing surface	Shear strain	2.5	2.4	0.40	Konstantinidis et al. (2008)
			Shear key			
DS1	Gap closure	Displacement [mm] (in)	50 (2.00)	50 (2.00)	0.20	
DS2	Formation of weak plane and small off-centering	Displacement [mm] (in)	60 (2.36)	60 (2.36)	0.40	Bozorgzadeh et al. (2006)
DS3	Significant off-centering	Displacement [mm] (in)	72 (2.85)	72 (2.85)	0.40	Bozorgzadeh et al. (2006)
DS4	Shearing off (failure)	Displacement [mm] (in)	87 (3.42)	87 (3.42)	0.30	Bozorgzadeh et al. (2006)
			Backwall			
DS1	Joint seal assembly damage	Displacement [mm] (in)	38 (1.50)	16 (0.75)	0.20	Caltrans (1994)
DS2	Gap closure	Displacement [mm] (in)	50 (2.00)	25 (1.00)	0.20	Caltrans (1994)
DS3	Formation of slip plane at backfill	Displacement [mm] (in)	70 (2.77)	54 (2.12)	0.40	Bozorgzadeh (2007)
DS4	Backwall shearing off	Displacement [mm] (in)	109 (4.30)	111 (4.36)	0.40	Bozorgzadeh (2007)

226

227   Table S5 presents DSs assumed for superstructure. In addition, collapse due to unseating

228   occurs when the superstructure displaces in longitudinal direction from the stemwall of abutment.

229   The seat width for the prototype bridges is 762 mm (30 in) (Caltrans 2013). Hence, accounting for

230   the gap between backwall and superstructure, the superstructure can displace 711 mm (28 in) and

231   737 mm (29 in) for PB1 and PB2, respectively, before it unseats.

232

233

Table S5. Superstructure damage states

DS	Qualitative description	EDP	Median threshold	Log. (ln) st. dev. of threshold	Reference
DS1	Microcracks forming due to concrete crushing	Compressive strain at extreme fibers	0.002	0.40	Moehle (2015)
DS2	Flexural cracks	Tensile strain at extreme fibers	0.00013	0.34	ACI (1992)

234

235 *Section S6: Abutment and superstructure repairs*

236 The repair methods for abutments are summarized in Table S6 and superstructure repair

237 methods are summarized in Table S7. Note that contact area (used for surface repairs) refer to

238 contact area of both abutment element and superstructure, i.e. 10% of contact area refers to 10%

239 of contact area of shear key and 10% of contact area of superstructure. The excavation areas for

240 backwall DS3 and 4 are shown in Fig. S7.

241 **Table S6.** Abutment repair methods

DS	Repair	Reference
Bearing		
DS1	Bearing replacement	Konstantinidis et al. (2008)
Shear key		
DS1	Surface repair (10% of contact area)	
DS2	Surface repair (50% of contact area), re-centering	
DS3	Shear key replacement	Bozorgzadeh et al. (2006)
DS4	Shear key replacement	Bozorgzadeh et al. (2006)
Backwall		
DS1	Joint seal assembly and blockouts, or seal replacement	Caltrans (1994)
DS2	Joint seal assembly and blockouts, or seal replacement, surface repair (10% of contact area)	Caltrans (1994)
DS3	Backfill replacement, patching of backwall	Bozorgzadeh (2007)
DS4	Backfill replacement, backwall replacement, approach slab replacement	Bozorgzadeh (2007); Mackie et al. (2011)

242

244   (a)   (b)   (c)
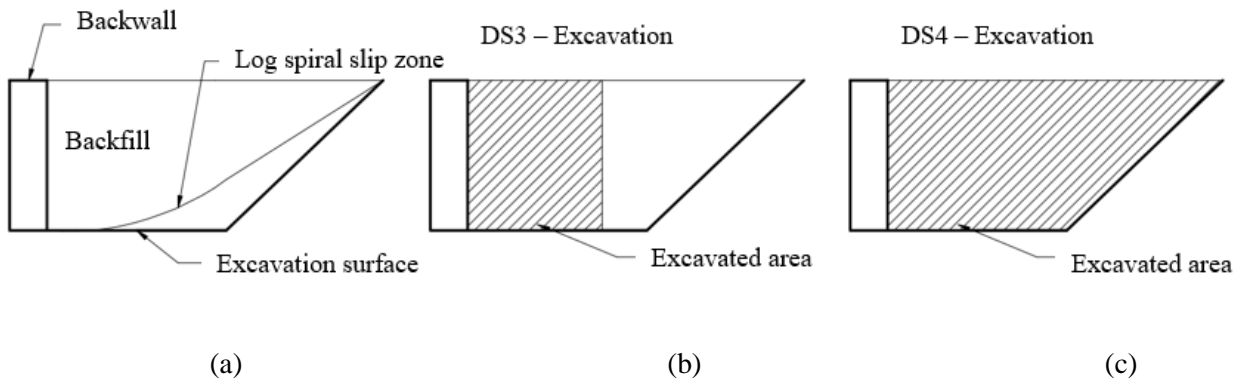245 **Fig. S7.** Excavation required for backwall repairs showing: (a) simplified excavation surface, (b)
246 excavated area for DS3, and (c) excavated area for DS4
247
248 Cracking in the superstructure can occur either due to flexure (tensile cracking) or due to

249 compression. The flexural cracks form when the concrete reaches the strain associated with the

250 peak tensile strength (ACI 1992). In compression, microcracks due to crushing can form when

251 concrete reaches its ultimate strength (Moehle 2015).

252 **Table S7.** Superstructure repair methods

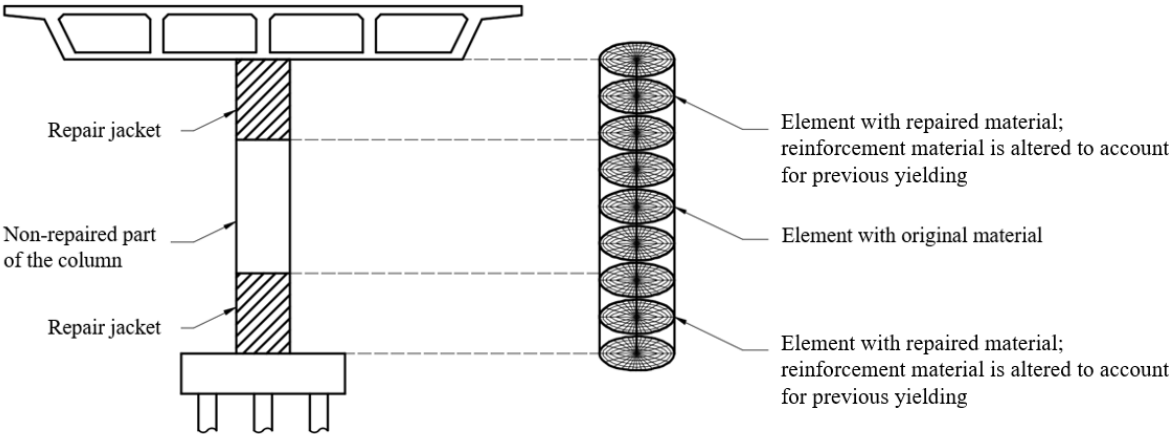| DS	Repair	Reference
DS1	30% of superstructure surface treated with methacrylate	Mackie et al. (2007)
DS2	Epoxy injections over 30% of surface	Mackie et al. (2007)

253

254

255 **Fig. S8.** Nonlinear model of repaired column

256 *Section S7: Material unit costs*

257 Unit costs of materials used in this study are presented in Table S8. Unless otherwise noted,

258 the data were collected from Caltrans project bids (Caltrans 2017b). Costs published before the

259 first quarter of 2017 are adjusted to 2017 dollars based on Caltrans cost index data.

260 The total costs for new construction of PB1 and PB2 in 2017 dollars are \$3,520,100 and

261 \$4,650,800, respectively (Caltrans 2017a; Ketchum et al. 2004).

262 **Table S8.** Material costs

	Unit	Min. quantity	Max. cost (\$)	Dispersion *	Max. quantity	Min. cost (\$)	Dispersion	# of points **
Remove unsound concrete	m^3	0.2	21081	0.67	5	1619	0.49	35
Reinforcing steel	kg	1030	5	0.47	8376	2	0.24	41
Steel casing	kg	NA	15	0.24				9
Rapid setting concrete	m^3	0.8	8990	0.31	15	510	0.5	29
Shotcrete	m^3	NA	102	0.33				12
Headed bars	EA	192	30	0.24	445	12	0.53	19
Structural concrete	m^3	89	3816	0.48	849	1052	0.38	48
Core concrete	m	NA	951	0.45				12
Repair spalled surface	m^2	4	3816	0.57	16	824	0.56	21
Inject epoxy	m	NA	400	0.44				10
Post-tension strand	kg	NA	60	0.50				***
Retrolock	EA	NA	92	0.50				***
CFRP Wrap	m^2	NA	215	0.40				****
Drill and bond dowel	m	83	166	0.58	125	110	0.25	24
Temporary support	kN	NA	10	0.20				8
Bridge removal - Column	m^3	NA	6235	0.50				*****
Bridge removal - Other	m^3	NA	1831	0.50				*****
Bearing	EA	NA	1949	0.52				4
Excavation	m^3	110	429	0.51	1013	45	0.55	36
Backfill	m^3	147	266	0.49	526	119	0.49	37
Joint seal assembly	m	NA	1225	0.43				32
Concrete - approach slab	m^3	53	2293	0.21	182	1325	0.34	38
Aggregate base	m^3	NA	442	0.58				30
Prepare deck	m^2	678	18	0.55	13510	2	0.32	67
Methacrylate	1	3153	17	0.45	6003	13	0.27	49
Treat deck	m^2	2058	6	0.44	5476	3	0.36	47

263   *   The dispersion of the material quantities between the maximum and minimum amount sis assumed to

264   linearly vary with quantity between the dispersion value at maximum cost and the dispersion value at minimum cost.

265   **   Number of data points used to perform segmented regression

266   ***   Cost from Sarrazin (2004)

267   ****   Cost from Cady (personal correspondence, 2017), and market research

268   *****   Cost from Mackie et al. (2011)

269

270   *Section S8: Hazard curve for Orange, CA site*

271   Both bridges are assumed to be located at the location of the La Veta Overcrossing in Orange,

272   Ca (Lat. 33.781, Long. -117.831). To compute seismic hazard curves for the selected IM, this

273   study follows the procedure outlined by Eads et al. (2015). The analysis considers a majority of

274   seismic sources at the site, as identified by USGS unified hazard tool (USGS 2018), *i.e.* those

275   sources contributing to over 90% of seismic hazard on the site. First, for each source scenario, the

276   median and logarithmic standard deviations of Sa for selected periods in the period range used to

277   obtain Sa_{avg} are calculated using a ground motion prediction equation. The authors used the Boore

278   at al. (2014) ground motion prediction equation; this equation was selected for ease of

279   implementation. For each period in the period region of Sa_{avg}, the Sa distribution is calculated by

280   combining values from the ground motion prediction equation and their contribution to seismic

281   hazard. Then, the median and logarithmic standard deviation values of $\overline{Sa_{avg}}$ for given site are

282   determined using correlation coefficients for Sa values of different periods and directions (Baker

283   and Jayaram 2017). The calculated hazard curve is shown in Fig. S9.

284
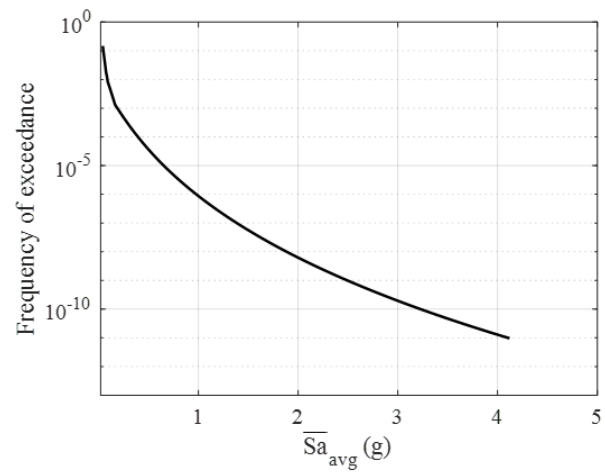
285

286   **Fig. S9.** Hazard curve for location of PB2

287

288   *Section S9: Probabilistic treatment of the cost curve*

289   To treat the cost curve probabilistically, first, a random number, θ, out of normal distribution

290   with mean of 0, and standard deviation of 1 is generated. This θ is then used to multiply standard

291   deviation of the cost curve at each discrete value of IM. This process creates a random realization

292   of the entire cost curve. (The underlying assumption, here, is that the repair costs values for each

293   IM are perfectly correlated – hence using one θ for all IMs in one realization. This assumption is

294   most likely not true, however it showed to be the most conservative approach in treating the

295   uncertainty.)

296

297 **References**

298 AASHTO. (2011). *AASHTO Guide Specifications for LRFD Seismic Bridge Design (2nd Edition)*

299 *with 2012, 2014 and 2015 Interim Revisions*. Washington, DC.

300 ACI (American Concrete Institute). (1992). "Report on High-Strength Concrete." *ACI Manual of*

301 *Concrete Practice No. 363R-92*, Farmington Hills, MI.

302 Aviram, A., Mackie, K. R., and Stojadinovic, B. (2008). "Guidelines for Nonlinear Analysis of

303 Bridge Structures in California." *No. PEER 2008/03,* Pacific Earthquake Engineering

304 Research Center.

305 Bae, S., Mieses, A. M., and Bayrak, O. (2005). Inelastic Buckling of Reinforcing Bars. *Journal of*

306 *Structural Engineering*, *131*(2), 314–321, 10.1061/(ASCE)0733-9445(2005)131:2(314).

307 Baker, J. W., and Jayaram, N. (2017). "Correlation of spectral acceleration values from NGA

308 ground motion models." *Earthquake Spectra*, *24*(1), 299–317.

309 Bayrak, O., and Sheikh, S. A. (2001). "Plastic Hinge Analysis." *Journal of Structural Engineering*,

310 *127*(9), 1092–1100, 10.1061/(ASCE)0733-9445(2001)127:9(1092).

311 Boore, D. M., Stewart, J. P., Sayhan, E., and Atkinson, G. M. (2014). "NGA-West2 Equations for

312 predicting PGA, PGV, and 5% damped PSA for shallow crustal earthquakes." *Earthquake*

313 *Spectra*, *30*(3), 1057–1085.

314 Bozorgzadeh, A. (2007). "Effect of Structure Backfill on Stiffness and Capacity of Bridge

315 Abutments." *PhD Thesis,* University of California, San Diego.

316 Bozorgzadeh, A., Megally, S., Restrepo, J. I., and Ashford, S. A. (2006). "Capacity Evaluation of

317 Exterior Sacrificial Shear Keys of Bridge Abutments." *Journal of Bridge Engineering*,

318 *11*(5), 555–565, 10.1061/(ASCE)1084-0702(2006)11:5(555).

319 Caltrans. (1994). *Memo to Designers 7-10*, California Department of Transportation, Sacramento,

320   CA.

321   Caltrans. (2013). *Caltrans Seismic Design Criteria Version 1.7,* California Department of

322   Transportation, Sacramento, CA.

323   Caltrans. (2017a). "Contract Cost Data." < from

324   http://sv08data.dot.ca.gov/contractcost/index.php> (September 14, 2017)

325   Caltrans. (2017). "Project Bucket Search." <from http://www.dot.ca.gov/des/oe/project-bucket-

326   output.php> (September 14, 2017)

327   Dhakal, R. P., and Maekawa, K. (2002). "Reinforcement Stability and Fracture of Cover Concrete

328   in Reinforced Concrete Members." *Journal of Structural Engineering*, *128*(10), 1253–

329   1262, 10.1061/(ASCE)0733-9445(2002)128:10(1253)

330   Eads, L., Miranda, E., and Lignos, D. G. (2015). "Average Spectral Acceleration as an Intensity

331   Measure for Collapse Risk Assessment." *Earthquake Engineering and Structural*

332   *Dynamics*, *44*(12), 2057–2073.

333   FHWA. (2015). "National Bridge Inventory." <from

334   https://www.fhwa.dot.gov/bridge/nbi/ascii.cfm> (October 15, 2016)

335   Goodco Z-Tech. (2015). "Elastomeric Bearings." <https://www.canambridges.com/wp-

336   content/uploads/2015/11/goodco-z-tech-elastomeric-bearings.pdf> (May 9, 2017)

337   Jiang, T., and Teng, J. G. (2007). "Analysis-Oriented Stress-Strain Models for FRP-Confined

338   Concrete." *Engineering Structures*, *29*(11), 1698–3968.

339   Kashani, M. M., Lowes, L. N., Crewe, A. J., and Alexander, N. A. (2016). "Nonlinear Fibre

340   Element Modelling of RC Bridge Piers Considering Inelastic Buckling of Reinforcement."

341   *Engineering Structures*, *116*, 163–177.

342   Ketchum, M., Chang, V., and Shantz, T. (2004). "Influence of Design Ground Motion Level on

343   Highway Bridge Costs." *Report No. 6D01*, Pacific Earthquake Engineering Research

344   Center.

345   Konstantinidis, D., Kelly, J. M., and Makris, N. (2008). "Experimental Investigation on the seismic

346   response of bridge bearings." *Repost No. EERC 2008-02*, Earthquake Engineering

347   Research Center, Univerisity of California.

348   Luco, N., and Cornell, C. A. (2007). "Structure-Specific Scalar Intensity Measures for Near-

349   Source and Ordinary Earthquake Ground Motions." *Earthquake Spectra*, *23*(2), 357–392.

350   Mackie, K. R., and Stojadinovic, B. (2004). "Improving Probabilistic Seismic Demand Models

351   Through Refined Intensity Measures." *Proc., 13th World Conference on Earthquake*

352   *Engineering*. Vancouver, B.C., Canada.

353   Mackie, K. R., Wong, J.-M., and Stojadinovic, B. (2008). "Integrated Probabilistic Performance-

354   Based Evaluation of Benchmark Reinforced Concrete Bridges." *Repost No. PEER*

355   *2007/09*, Pacific Earthquake Engineering Research Center.

356   Mackie, K. R., Wong, J.-M., and Stojadinovic, B. (2011). "Bridge Damage and Loss Scenarios

357   Calibrated by Schematic Design and Cost Estimation of Repairs." *Earthquake Spectra*,

358   *27*(4), 1127–1145.

359   Mander, J. B., Priestley, M. J. N., and Park, R. (1988). "Theoretical Stress-Strain Model for

360   Confined Concrete." *Journal of Structural Engineering*, *114*(8), 1804–1826,

361   10.1061/(ASCE)0733-9445(1988)114:8(1804).

362   Mander, J. B., Panthaki, F. D., and Kasalanati, A. (1994). "Low-Cycle Fatigue Behavior of

363   Reinforcing Steel." *Journal of Materials in Civil Engineering*, *6*(4), 453–468,

364   10.1061/(ASCE)0899-1561(1994)6:4(453).

365   Moehle, J. P. (2015). *Seismic Design of Reinforced Concrete Buildings*, McGraw Hill Education,

366   New York City, NY.

367   Murcia-Delso, J. (2013). "Bond-Slip Behavior and Development of Bridge Column Longitudinals

368   Reinforcing Bars in Enlarged Pile Shafts." *PhD Thesis*, University of California, San

369   Diego.

370   Padgett, J. E., Nielson, B. G., and DesRoches, R. (2008). "Selection of Optimal Intensity Measures

371   in Probabilistic Seismic Demand models of highway Bridge Portfolios." *Earthquake*

372   *Engineering and Structural Dynamics*, *37*(5), 711–725.

373   Salehi, M., and Sideris, P. (2017). "Refined Gradient Inelastic Flexibility-Based Formulation for

374   Members Subjected to Arbitrary Loading." *Journal of Engineering Mechanics*, *143*(9),

375   10.1061/(ASCE)EM.1943-7889.0001288, 04017090.

376   Sarrazin, J. (2004). "A Comparative Analysis of Seismic Retrofit Techniques for Reinforced

377   Concrete Bridge Columns." *Master's Thesis*, University of Ottawa.

378   Sideris, P., and Salehi, M. (2016). "A Gradient Inelastic Flexibility-Based Frame Element

379   Formulation." *Journal   of   Engineering   Mechanics*,   *142*(7),

380   https://doi.org/10.1061/(ASCE)EM.1943-7889.0001083, 04016039.

381   Spoelstra, M. R., and Monti, G. (1999). "FRP-Confined Concrete Model." *Journal of Composites*

382   *for Construction*, *3*(3), 143–150, 10.1061/(ASCE)1090-0268(1999)3:3(143).

383   Stewart, J. P., Taciroglu, E., and Wallace, J. W. (2007). "Full Scale Cyclic Testing of Foundation

384   Support Systems for Highway Bridges. Part II: Abutment Backwalls." *Report No. UCLA-*

385   *SGEL 2007/02*, University of California, Los Angeles.

386   USGS. (2018). *Unified Hazard Tool,* <https://earthquake.usgs.gov/hazards/interactive/>

387